**Showcasing the study of lithium ion batteries by the group of Prof. Chunli Guo, College of Materials Science and Engineering, Taiyuan University of Technology, China.**

Title: Well-shaped Mn_3O_4 tetragonal bipyramids with good performance for lithium ion batteries

Well-shaped Mn_3O_4 tetragonal bipyramids with a reversible capacity and a stable coulomb efficiency have been synthesized by a simple approach. The formation mechanism of the Mn_3O_4 tetragonal bipyramids from $MnCO_3$ and $MnOOH$ was discussed in detail from the viewpoint of crystallography.

As featured in:
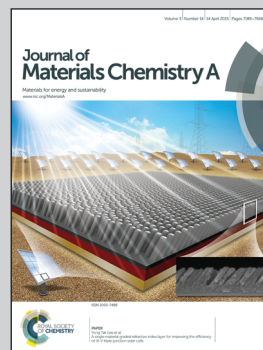
Journal of
Materials Chemistry A

ROYAL SOCIETY
OF CHEMISTRY

www.rsc.org/MaterialsA

PAPER

Well-shaped Mn₃O₄ tetragonal bipyramids with good performance for lithium ion batteries†

Taotao Li,[a] Chunli Guo,*[a] Bo Sun,[b] Ting Li,[a] Yonggang Li,[a] Lifeng Hou[a] and Yinghui Wei*[ac]

Well-shaped Mn₃O₄ tetragonal bipyramids with a high reversible capacity of 822.3 mA h g⁻¹ are synthesized by a simple hydrothermal method without any surfactants or coordination compounds. The structural features and morphology of the final product are investigated by X-ray diffraction (XRD), scanning electron microscopy (SEM) and high-resolution transmission electron microscopy (HRTEM). The SEM and HRTEM results reveal that all the eight exposed facets of the Mn₃O₄ tetragonal bipyramids are indexed to the high-energy {101} planes. The tetragonal bipyramids with high-energy facets provide the Mn₃O₄ anode material with a high initial discharge capacity (1141.1 mA h g⁻¹). In addition, the anode displays a good fast rate performance, delivering a reversible capacity of 822.3 mA h g⁻¹ (the theoretical capacity: 937 mA h g⁻¹) at a current density of 0.2 C after 50 cycles. Moreover, the coulomb efficiency for the first cycle reaches about 66% and remains at about 100% during the subsequent cycles. A relatively detailed growth mechanism of these tetragonal bipyramids is proposed in this manuscript.

1. Introduction

Lithium ion batteries have attracted significant attention because of their high power density (150 Wh kg⁻¹) and high energy density (400 Wh L⁻¹).[1–3] They exhibit great prospects in small portable applications including mobile phones, notebook computers, digital cameras, and other fields such as submarines, aerospace, and electric vehicles. As known, graphite-based materials as the main lithium ion battery anodes have been industrialized. However, graphite-based materials have a limited theoretical specific capacity of 372 mA h g⁻¹ and a quick capacity fade caused by the disintegration, which cannot meet the broad needs of high-energy applications.[4–6] Therefore, alternative anode materials with higher energy capabilities are urgently needed. Nanomaterials have gradually attracted attention in the application of lithium ion batteries due to their very large specific surface areas, short ion diffusion paths, creep resistance and high plasticity.

Nano-sized transition metal oxides have also been considered as promising alternative anode materials owing to their high theoretical specific capacity (450–1500 mA h g⁻¹).[7,8] Among the transition oxides, Mn₃O₄ is worth exploiting, not only

because of its high theoretical capacity of 937 mA h g⁻¹, but also due to its good properties of low toxicity, low cost and abundance in nature.[9–11] In addition, Mn₃O₄ exhibits better thermo-stability than graphite-based materials when batteries are overcharged or charged at a high rate.[9,12] It is generally accepted that lower redox potentials render higher energy density anode materials. Mn₃O₄ with a lower redox potential (1.2 V), has been found to be more fascinating than other transition metals such as cobalt (2 V).[11,13] Thus, considerable efforts have been put into the area of Mn₃O₄ anode materials in the recent years.

To obtain the excellent properties of Mn₃O₄ nanoparticles, many investigations focused on the size control and morphology control of Mn₃O₄ nanomaterials. For instance, mesoporous Mn₃O₄ nanotubes delivering a reversible capacity of 641 mA h g⁻¹ at a high current density of 500 mA g⁻¹ were reported by Bai.[13] Single crystalline Mn₃O₄ nano-octahedra were synthesized by a hydrothermal method and their electro-chemical results show a charge capacity of 500 mA h g⁻¹ at a current density of 50 mA g⁻¹ and a charge capacity of 350 mA h g⁻¹ when cycled at 500 mA g⁻¹.[14] Mn₃O₄ nano-octahedra prepared by the calcination of a Zn–Mn citrate complex can exhibit a reversible capacity of about 240 mA h g⁻¹ at a high rate of 1000 mA g⁻¹.[15] Mn₃O₄ octahedral nanocrystals were also prepared by a hydrothermal method and their cycle performances exhibited a discharge capacity of 269 mA h g⁻¹ at a current density of 500 mA g⁻¹.[16] The above-mentioned experimental results showed that they were still far from the theoretical capacity of 937 mA h g⁻¹.

In this study, we report a surfactant-free hydrothermal method to fabricate well-shaped Mn₃O₄ tetragonal bipyramids

[a]College of Materials Science and Engineering, Taiyuan University of Technology, Taiyuan, Shanxi, 030024, P. R. China. E-mail: guochunli@tyut.edu.cn; weiyinghui@tyut.edu.cn; Tel: +86 351 6018683

[b]Department of Mechanical Engineering, National University of Singapore, 119260, Singapore

[c]Lvliang College, Lishi, Shanxi 033000, China

with a high reversible capacity using $KMnO_4$ and $H_2C_2O_4 \cdot 2H_2O$ as raw materials at 200 °C for 10 h. High-resolution transmission electron microscope (HRTEM) data indicated that the eight exposed facets of the Mn_3O_4 tetragonal bipyramids were the {101} planes. The electrochemical performance of the Mn_3O_4 tetragonal bipyramids as an anode material was evaluated by cyclic voltammetry (CV) and galvanostatic discharge–charge tests. The electrochemical results indicate that the Mn_3O_4 tetragonal bipyramids exhibit a high initial discharge capacity (1141.1 mA h g^{-1}) and deliver a reversible capacity of 822.3 mA h g^{-1} at a current density of 0.2 C after 50 cycles, which reaches ∼88% of the theoretical capacity of manganese oxides. The coulomb efficiency for the first cycle reaches about 66% and remains at about 100% during the subsequent cycles. Finally, the formation mechanism of the Mn_3O_4 tetragonal bipyramids is discussed from the viewpoint of crystallography.

2. Experimental section

2.1 Synthesis of the Mn_3O_4 tetragonal bipyramids

$KMnO_4$ and $H_2C_2O_4 \cdot 2H_2O$ (99%) were purchased and used without any further purification. In a typical procedure, $KMnO_4$ (0.50 g) was completely dissolved in 40 mL KOH solution (0.01 M) to form a dark purple solution. $H_2C_2O_4 \cdot 2H_2O$ (0.86 g) was added to the above solution. Then, the mixed solution was transferred to a Teflon-lined stainless steel autoclave (60 mL), which was subsequently sealed and maintained at 200 °C for 10 h and then cooled to room temperature. The brownish red product was collected and washed with distilled water and absolute ethanol several times. Finally, the product was dried under vacuum at 60 °C for several hours.

2.2 Characterization

The phase of the products was characterized by X-ray powder diffraction (XRD) technique using a Bruker D8 advanced X-ray diffractometer equipped with a graphite-monochromatized Cu-Kα radiation (Kα = 1.5418 Å). The X-ray photoelectron spectroscopy (XPS) spectra of the synthesized Mn_3O_4 tetragonal bipyramids were obtained with an Axis Ultra, Kratos (UK) using monochromatic Al Kα radiation (150 W, 15 kV, and 1486.6 eV). Scanning electron microscopy (SEM) images were obtained with a MIRA3 LMH scanning electron microscope. The TEM and HRTEM images were recorded using a JEOL-2100 high-resolution transmission electron microscope at an acceleration voltage of 200 kV.

2.3 Electrochemical measurements

The working electrodes for the measurement of electrochemical properties were prepared with 70 wt% active materials of the Mn_3O_4 tetragonal bipyramids, 20 wt% conducting acetylene black, and 10 wt% carboxy methyl cellulose (CMC) binder in water. The slurry was pasted on a clean copper foil followed by drying in vacuum at 80 °C for 12 h. The resulting foil was roll-pressed and cut into a disc. The Mn_3O_4 tetragonal bipyramid cells were fabricated using lithium foil as both a counter electrode and a reference electrode, Celgard 2400 as a separator,

and a solution of 1 M $LiPF_6$ in a mixture of ethylene carbonate (EC) and dimethyl carbonate (DMC) (1 : 1 by volume) as the electrolyte. The cells were assembled in an argon-filled humidity-free glove box. The cells were charged and discharged from 0.01 to 3.0 V at different current rates (Land CT 2001A). CV profiles were obtained in the range of 0.01–3 V at a scanning rate of 0.1 mV s^{-1} from an electrochemical workstation (CHI-760).

3. Result and discussion

The as-prepared product was characterized by XRD (Fig. 1 and S1†). In Fig. 1, almost all the diffraction peaks of the as-synthesized sample can be well indexed to the tetragonal structure of Mn_3O_4 with lattice parameters of $a = b = 5.763$ Å and $c = 9.456$ Å, which is in good agreement with the data reported in the JCPDS standard card (no. 89-4837, space group $I4_1/amd$ (141)). The valency of the Mn_3O_4 was analyzed by X-ray photoelectron (XPS) spectroscopy. The XPS spectra in Fig. S2† indicate that the Mn2p region consists of a spin–orbit doublet (L–S coupling) with binding energies of 652.9 eV ($Mn2p_{1/2}$) and 642.1 eV ($Mn2p_{3/2}$) for the Mn_3O_4 tetragonal bipyramids, which is characteristic of a mixed-valence manganese system (Mn^{3+} and Mn^{2+}).[17]

The SEM image (Fig. 2a) shows that the morphologies of the final sample are Mn_3O_4 tetragonal bipyramids. Fig. 2b is a high-magnification SEM image of the Mn_3O_4 tetragonal bipyramids. It can be clearly observed that the surfaces of the well-defined Mn_3O_4 tetragonal bipyramids are mostly smooth. The inset in Fig. 2b is an ideal geometrical model of the Mn_3O_4 tetragonal bipyramids. We defined the vertex of the long axis (C_4) as A and the vertex of the minor axis (C_2) of the Mn_3O_4 tetragonal bipyramids as B or C. To obtain a closer insight of the inner structure of the well-defined Mn_3O_4 tetragonal bipyramids, TEM was carried out. Fig. 2c and d are the low-magnification and high-magnification TEM images, respectively. In Fig. 2c, it can be observed that there are two types of morphologies, including square and rhombus, which are slightly different from the results observed from the SEM. The reason was that
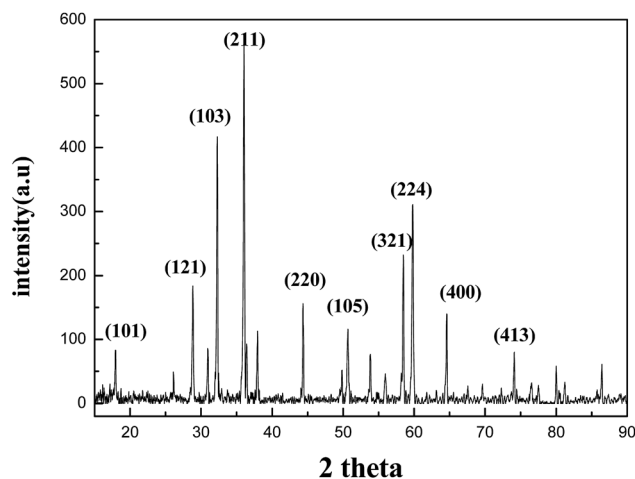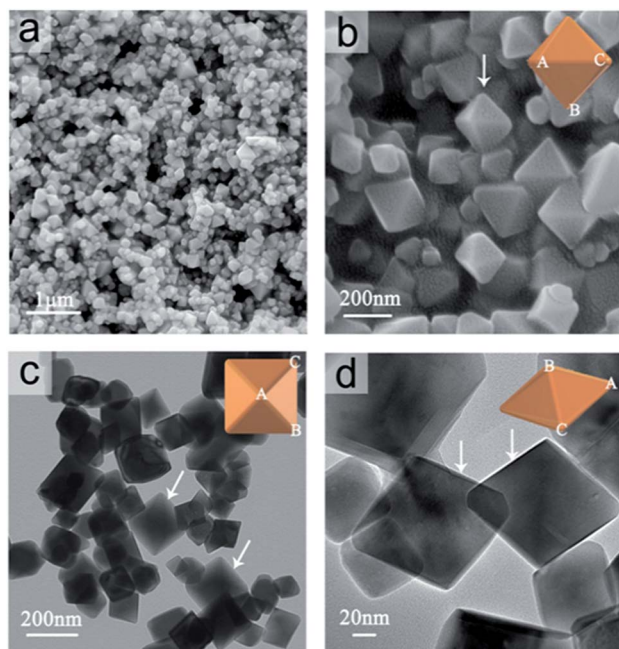

Fig. 1 XRD pattern of the as-prepared product.

Fig. 2 A typical large-area SEM image (a) and a partially enlarged SEM image (b) of the Mn_3O_4 tetragonal bipyramids; a large-area TEM image (c) and an enlarged TEM image (d) of the Mn_3O_4 tetragonal bipyramids. The insets in b, c and d are the ideal geometrical models of the Mn_3O_4 tetragonal bipyramids marked with the corresponding white arrows, in which the ratio of AB and BC is about 1 : 1.

Fig. 3 (a) A typical TEM image of the Mn_3O_4 tetragonal bipyramids; (b) the corresponding selected area electron diffraction (SAED) pattern; (c) the corresponding simulated 2D geometrical model image along the *Y* axis; (d) the corresponding 3D geometrical model image; (e) an HRTEM image of the white rectangle marked with e in (a), the angle between the two opposite planes is 63°; (f) a HRTEM image of the white rectangle marked with f in (a), the angle between the two adjacent planes is 117°.

these two morphologies were the projections of tetragonal bipyramids from different perspectives. The inset in Fig. 2c is an ideal geometrical model of Mn_3O_4 tetragonal bipyramids from the view of A, whose projection is a square with a dark crossing (marked with the white arrows). If viewed from the midpoint of AB in the geometrical model of Fig. 2d, the projection of the Mn_3O_4 tetragonal bipyramid labeled with the white arrows can become a rhombus. Based on our limited SEM observation along with a low resolution survey, it is estimated that up to about 95% of the Mn_3O_4 tetragonal bipyramids and their average sizes (Heywood diameter) range from 80 to 160 nm.

To further investigate the detailed microstructure of the Mn_3O_4 tetragonal bipyramids, high-resolution TEM imaging was used. Fig. 3a is a typical TEM image of a whole Mn_3O_4 tetragonal bipyramid, and Fig. 3c and d are the corresponding simulated geometrical model images along different directions. The diffraction spots of the SAED pattern in Fig. 3b are in a regular sequence, which is a feature of a monocrystal. The facets are best revealed by the projection of the Mn_3O_4 tetragonal bipyramid along the [010] orientation, parallel to which 4 of the 8 exposed facets are imaged edge-on in Fig. 3a. The Miller indices of the exposed faces of the Mn_3O_4 tetragonal bipyramids can be confirmed by the conjunction of the angles between the facets in Fig. 3a, whose borders can be recognized as the projection of four {101} facets parallel to the [010] orientation.[18] The HRTEM images in Fig. 3e and f recorded from the white rectangle areas of Fig. 3a show continuous lattice fringes with a lattice spacing of 0.49 nm, which corresponds to the {101}
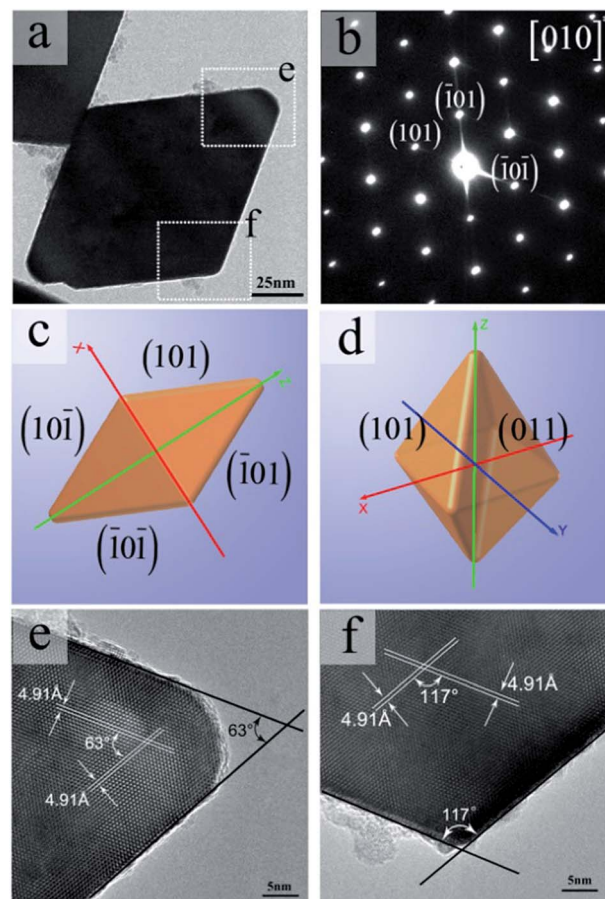
planes of Mn_3O_4. As shown in Fig. 3e, the angle of the two opposite surfaces ((101) and ($\bar{1}$01)) of 63° is measured, which is in good agreement with the angle marked with a black double-headed arrow in Fig. 3d. From Fig. 3f, it can be calculated that the angle between ($\bar{1}$01) and ($\bar{1}$0$\bar{1}$) is 117°, in accordance with the angle marked with the white double-headed arrow in Fig. 3f. Based on the above-mentioned crystal data, the crystal orientation relation to the morphology can be determined in Fig. 3c. Therefore, we drew a conclusion that the crystal facets at the surface of the Mn_3O_4 tetragonal bipyramids are in accordance with the {101} planes.

As an effort to explore the growth mechanism for this synthetic route, it is necessary to assess the morphology and structure of samples prepared at various reaction times while other conditions are kept the same. Fig. 4a shows an SEM image of the products synthesized for 4 h. From Fig. 4a, two distinct morphologies were observed. One is aggregated micron-sized cubic-shaped nanoparticle and the other is one-dimensional nanocrystal. Further SEM structural analysis provides more
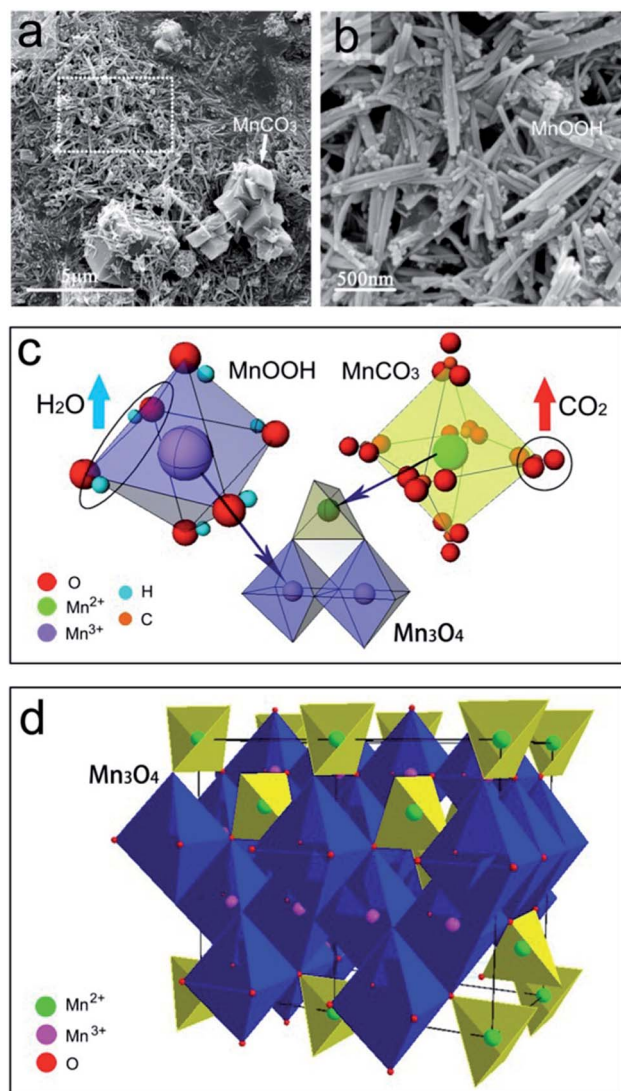
Fig. 4   (a) A SEM image and (b) a partially enlarged SEM image of the reaction process at 4 h; (c) a schematic illustration of the formation of the Mn_3O_4 tetragonal bipyramids and the transformation from $MnCO_3$ and MnOOH; (d) the crystal structure of the tetragonal Mn_3O_4 with two unit cells. The simulated diagrams of $MnCO_3$, MnOOH and Mn_3O_4 were extracted from the crystal files 9007689.cif, 9009774.cif and 1011262.cif respectively.

pronounced evidence to inspect the morphology of the white rectangle area in Fig. 4a. Fig. 4b is the typical SEM image of the one-dimensional nanocrystals. Rod-like structures with an average width of 45 nm and an aspect ratio of 4–20 are clearly observed. Moreover, the XRD data also show the presence of two major phases of $MnCO_3$ and MnOOH (Fig. S3†). According to the related studies, the chemical composition of the aggregated micron-sized cubic-shaped nanoparticles was $MnCO_3$ (ref. 19) and the chemical constitution of the rod-like structures was MnOOH.[20,21] Thus, the possible chemical reaction pathway involved in the range of 0 to 4 h can be written as follows:

$$KMnO_4 + H_2C_2O_4 + KOH \rightarrow$$
$$MnCO_3 + MnOOH + KHCO_3 + H_2O \quad (1)$$
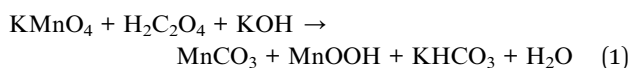
When the reaction time was increased to 6 h, Mn_3O_4 and MnOOH were indexed in the corresponding XRD (Fig. S4†). No obvious diffraction peaks of $MnCO_3$ were observed in the XRD pattern, which suggests that the $MnCO_3$ phase was an intermediate product. This interesting finding shows that the stability of $MnCO_3$ was not as good as that of MnOOH in our reaction route. It is common knowledge that the MnOOH phase is stable in a strong alkali solution (Fig. S5†). The SEM image of Fig. S6† also gives evidence that the aggregated cubic-shaped $MnCO_3$ nanoparticles disappeared and Mn_3O_4 tetragonal bipyramids emerged. When the reaction time was further increased from 6 to 8 h, the proportion of the Mn_3O_4 tetragonal bipyramids in the final products increased (Fig. S7†). When the reaction time was extended to 10 h, more than 95% Mn_3O_4 tetragonal bipyramids were inspected in our sample. Consequently, the chemical reactions involved in the growth from 4 to 10 h could be described as follows:

$$MnCO_3 + 2MnOOH \rightarrow Mn_3O_4 + CO_2 + H_2O \quad (2)$$
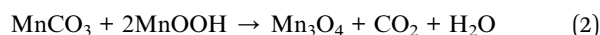
The reaction from 4 to 10 h can be summarized as a reaction diagram shown in Fig. 5. The overall reaction can be formulated as follows:

$$KMnO_4 + H_2C_2O_4 + KOH \rightarrow$$
$$Mn_3O_4 + CO_2 + KHCO_3 + H_2O \quad (3)$$
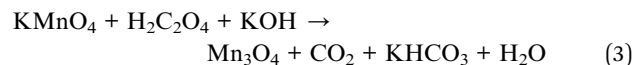
Furthermore, to elucidate the growth mechanism of these Mn_3O_4 tetragonal bipyramids, we proposed a hypothesis in the frame of a structural transformation from $MnCO_3$ and MnOOH to Mn_3O_4 on the basis of the above-mentioned reactions (Fig. 4c). As the structure of $MnCO_3$ was destroyed completely along with the escape of CO_2, the dissociative Mn^{2+} entered into the tetrahedral sites of the defective MnOOH cell. Then, the Mn_3O_4 spinel structure was formed. Fig. 4d presents the crystal structure of the tetragonal Mn_3O_4 with two unit cells. It is clearly displayed that the Mn_3O_4 structure has a normal spinel
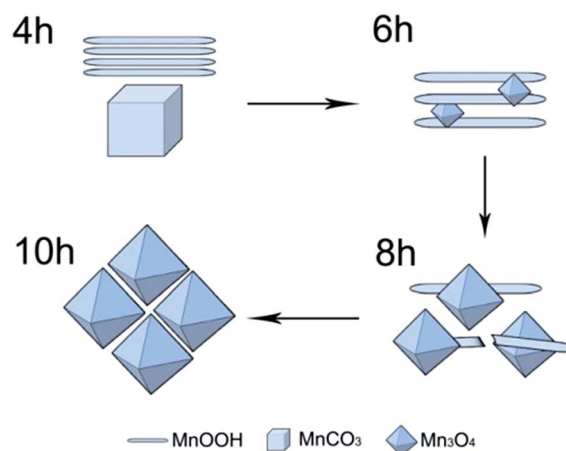

Fig. 5   A schematic illustration of the formation of the Mn_3O_4 tetragonal bipyramids.

structure with the Mn^{2+} ($4s^03d^5$) in the tetrahedral sites and Mn^{3+} ($4s^03d^4$) in the elongated octahedral sites,[22,23] which can be explained by the Jahn–Teller effect.[24] In the octahedral complexes of Mn_3O_4, the five 3d orbitals of the Mn atom in the Mn_3O_4 crystal structure are divided into two types: one is the t_{2g} orbital (d_{xy}, d_{zx} and d_{xy}), the other is the e_g^* orbital (d_z^2 and $d_{x^2-y^2}$).[25] Moreover, Mn^{3+} has a high-spin configuration of $(t_{2g})^3$ $(e_g^*)^1$. Every t_{2g} orbital (d_{xy}, d_{yz} and d_{zx}) has a 3d electron and the d_z^2 orbital of the e_g^* orbital is occupied by the remaining 3d electrons (Fig. S8†).[26] Four O^{2-} of the octahedral Mn_3O_4 complexes in the *XY* plane received a smaller repulsive force as compared to the two O^{2-} in the *Z* axis (Fig. S9†), resulting in the structure distortion from the octahedrons to the elongated tetragonal bipyramids. Furthermore, there are no compounds, such as surfactants and coordination compounds, which can affect the growth faces of the tetragonal bipyramids in our hydrothermal system. Accordingly, the final morphology of the as-prepared samples is consistent with its primary framework structure. Based on the HRTEM and SAED results, we know that the elongated octahedron structure stacked along the {101} planes simultaneously.

The electrochemical properties of the as-obtained Mn_3O_4 tetragonal bipyramids were first evaluated by CV. Fig. 6 displays three CV curves of the cell with the Mn_3O_4 tetragonal bipyramids used as the anode material under different cycles. In the first cathodic scan, two weak peaks appeared at 1.01 V (a) and 0.88 V (b); both vanished in the succeeding cycles. The peak (a) can be attributed to the reduction reaction ($Mn_3O_4 + 2Li^+ + 2e^- \rightarrow 3MnO + Li_2O$)[27] and the peak (b) can be ascribed to the formation of a solid electrolyte interphase (SEI) layer (electrolyte $+ e^- + Li^+ \rightarrow SEI(Li)$) on the surface of the Mn_3O_4 tetragonal bipyramid electrode.[14,28,29] In addition, the strong peak located at 0.08 V (c) is related to the reduction reaction of MnO (MnO $+ 2Li^+ + 2e^- \rightarrow Mn(0) + Li_2O$).[28] During the next anodic process, one peak located at 1.33 V (d) was observed due to an oxidation reaction of the former-formed Mn and the decomposition of Li_2O.[30] In the second cathodic cycle, the reduction peak shifts

from 0.08 V (c) to 0.32 V (e) which is mainly due to the irreversible phase transformation. After the second cycle, the appearance of similar CV curves indicates the good reversibility of the electrochemical reactions of the Mn_3O_4 tetragonal bipyramid electrode. On the basis of the above analysis results and the related literature,[31–33] the entire reversible electrochemical mechanism of Mn_3O_4 on Li insertion and extraction can be summarized by the following equation:

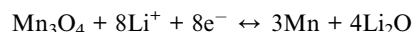$$Mn_3O_4 + 8Li^+ + 8e^- \leftrightarrow 3Mn + 4Li_2O$$

Fig. 7 exhibits the discharge and charge curves of the 1st, 2nd, 10th and 50th cycles for the Mn_3O_4 tetragonal bipyramid electrode cycled between 0.01 and 3 V at a current density of 0.2 C. In the first discharge curve (Li insertion), three distinctive regions (a, b and c) related to different Li storage mechanisms are observed. The first short plateau (a) and the following sloped region (b) can be assigned to the reduction reaction from Mn_3O_4 to MnO and the formation of the SEI film on the electrode surface, respectively. The long plateau (c) is related to the reduction reaction from Mn^{2+} to Mn^0.[27] In the first charge curve, a slight slope recorded between 1.1 and 1.5 V can be regarded as the oxidation reaction from Mn^0 to Mn^{2+} or Mn^{3+}.[27] All these results are in accordance with the CV test results. From the second cycle, the discharge plateau (d) of the Mn_3O_4 tetragonal bipyramid electrode shifts to about 0.5 V, indicating the irreversible formation of the crystalline metallic Mn and amorphous Li_2O matrix.[27] After the second cycle and even after 10th and 50th cycle, the discharge and charge curves are similar. However, nearly 7 mol of Li is stored per mole of Mn_3O_4 with a total capacity of 822 mA h g^{-1} during the 50th cycle, which is higher than that (760 mA h g^{-1}) of the 10th cycle.

Fig. 8 shows the cycling performance and the columbic efficiency of the Mn_3O_4 tetragonal bipyramid electrode at the
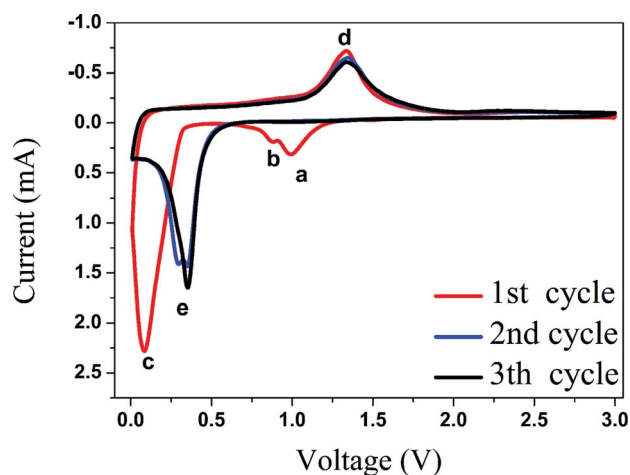

Fig. 6 CV curves of the Mn_3O_4 tetragonal bipyramid electrode at a constant density of 0.2 C in the voltage range of 0.01–3.0 V. The letters a–e denote the peaks.
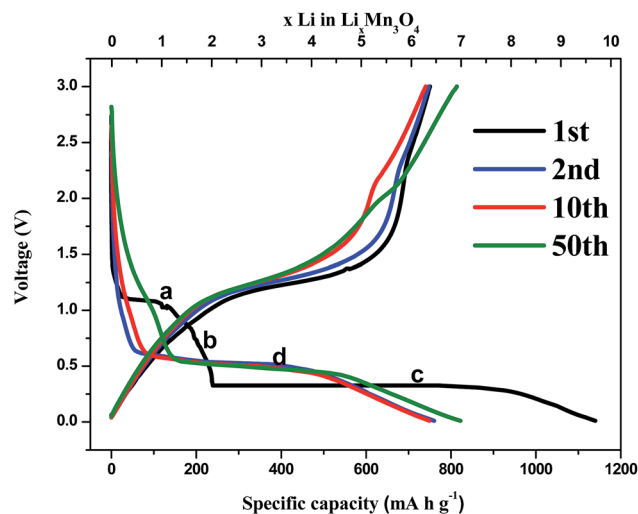

Fig. 7 The 1st, 2nd, 10th and 50th charge and discharge curves of the Mn_3O_4 tetragonal bipyramid electrode between 0.01 and 3 V at a current density of 0.2 C. The letters a–d represent the plateaus and the sloped regions.
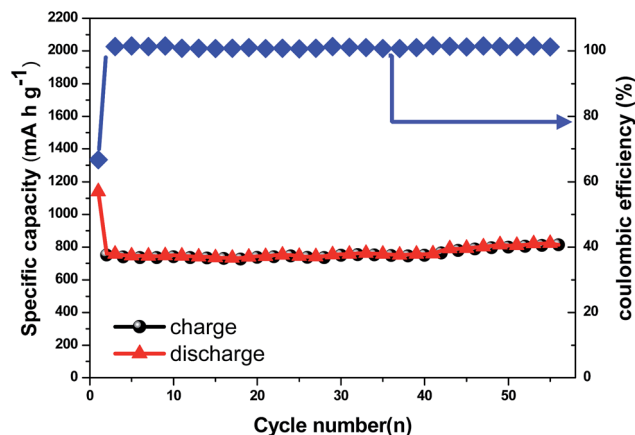
7252 | *J. Mater. Chem. A*, 2015, **3**, 7248–7254

This journal is © The Royal Society of Chemistry 2015

Fig. 8 Cycle performance and columbic efficiency *versus* cycle number of the Mn_3O_4 tetragonal bipyramid electrode at a current density of 0.2 C.

Fig. 9 The rate performance of the tetragonal bipyramid Mn_3O_4 electrode (rate = 0.1–2 C) and the cell was tested for 5 cycles at each current density.

rate of 0.2 C from 0.01 to 3.0 V after about 56 cycles. As shown in Fig. 8, the Mn_3O_4 tetragonal bipyramid electrode delivered an initial capacity of 1141.1 mA h g^{-1} and exhibited a first cycle columbic efficiency of 66.7%. The large irreversible capacity loss (33.3%) in the first cycle is very common for transition metal oxides, and the main reason is the formation of an SEI film by the degradation of the electrolyte (electrolyte + e$^-$ + Li$^+$ → SEI(Li)), the other is the transformation of irreversible phase (Mn nanoparticles and amorphous Li_2O matrix).[14,15,36] In the second cycle, its capacity quickly decreased to 761.1 mA h g^{-1} with an increased columbic efficiency of nearly 100%. In the subsequent cycles, the capacity and the columbic efficiency both remained steady. However, the capacity from the 20th to the 56th cycle gradually increased from 765.7 to 822.3 mA h g^{-1}. The growing reversible capacity can be explained by an interfacial mechanism in which extra lithium is accommodated in the boundary regions between the nano-sized Mn and Li_2O (in the reaction process, the sizes of these two products got smaller and the boundary regions increased) *via* charge separation.[34,35]

To evaluate the power capability of the Mn_3O_4 tetragonal bipyramid electrode, we investigated its rate performance at different current densities (Fig. 9). In Fig. 9, it can be observed that the reversible capacity gradually decreases as the current density increases. The specific capacities of 869, 798, 708 and 604 mA h g^{-1} are detected as the current density varies from 0.1, to 0.2, 0.5 and 1 C, respectively. Even at a current density as high as 2 C, the Mn_3O_4 tetragonal bipyramid electrode can still deliver an average specific capacity of 471 mA h g^{-1}, which is considerably higher than the theoretical specific capacity (372 mA h g^{-1}) of the graphite-based anode materials.[37] When the current density was back to 0.1 C, an average capacity could be recovered to 883 mA h g^{-1}, which was a little higher than the capacity (856.3 mA h g^{-1}) at the initial rate of 0.1 C.

The enhanced electrochemical performance of the as-synthesized Mn_3O_4 tetragonal bipyramids could be ascribed to its special structure. The nanoparticles provide a large specific surface area ((101) facets), which improves the utilization of the
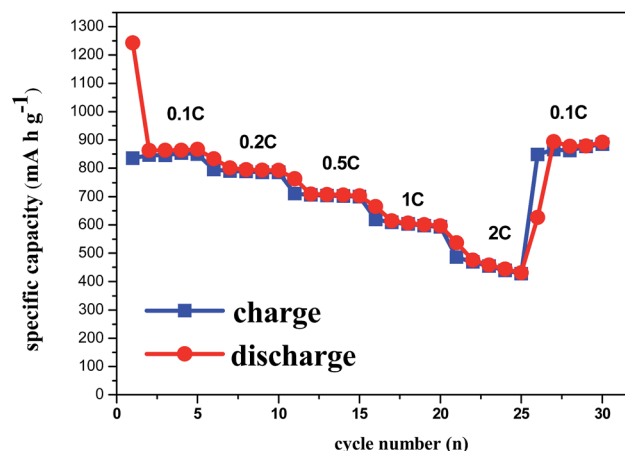
active material, and provides reduced transport pathways for lithium ions to transfer in and out easily. The structure of the Mn_3O_4 tetragonal bipyramids lithium ion batteries has the ability to tolerate volume deformation during the discharge–charge process and maintain the stability of the Mn_3O_4 electrode. These may be responsible for the good performance of LIBs.[13,36] Therefore, the Mn_3O_4 tetragonal bipyramid electrode with a good rate capacity can be regarded as a promising alternative anode material for lithium ion batteries.

4. Conclusion

Mn_3O_4 tetragonal bipyramids with a high reversible capacity (up to 822.3 mA h g^{-1}) were synthesized by the reaction of $KMnO_4$ and $H_2C_2O_4 \cdot 2H_2O$ in an alkali solution at 200 °C for 10 h without any surfactants or coordination compounds. The investigation by the HRTEM and SAED data of the final products showed that the Mn_3O_4 tetragonal bipyramids were monocrystals and the elongated octahedron structure of the Mn_3O_4 tetragonal bipyramids stacked along the {101} planes. The CV and the galvanostatic discharge–charge test results showed that the Mn_3O_4 tetragonal bipyramid electrode could display a high initial discharge capacity of 1141.1 mA h g^{-1} and deliver a reversible capacity of 822.3 mA h g^{-1}, which is close to the theoretical capacity value of 937 mA h g^{-1}, at 0.2 C after 50 cycles. The coulombic efficiency is nearly 100% after the first cycles. The growth mechanism of the Mn_3O_4 tetragonal bipyramids was proposed and it efficiently accounted for the obtained experimental results.

Acknowledgements

References

1 J. M. Tarascon and M. Armand, *Nature*, 2001, **414**, 359.

2 P. G. Bruce, B. Scrosati and J. M. Tarascon, *Angew. Chem., Int. Ed.*, 2008, **47**, 2930.

3 S. Goriparti, E. Miele, F. D. Angelis, E. D. Fabrizio, R. P. Zaccaria and C. Capiglia, *J. Power Sources*, 2014, **257**, 421.

4 T. H. Kim, J. S. Park, S. K. Chang, S. Choi, J. H. Ryu and H. K. Song, *Adv. Energy Mater.*, 2012, **2**, 860.

5 Y. Z. Jiang, M. J. Hu, D. Zhang, T. Z. Yuan, W. P. Sun, B. Xu and M. Yan, *Nano Energy*, 2014, **5**, 60.

6 Z. C. Bai, N. Fan, C. H. Sun, Z. C. Ju, C. L. Guo, J. Yang and Y. T. Qian, *Nanoscale*, 2013, **5**, 2442.

7 P. Poizot, S. Laruelle, S. Grugeon, L. Dupont and J. M. Tarascon, *Nature*, 2000, **407**, 496.

8 Z. Q. Li, N. N. Liu, X. K. Wang, C. B. Wang, Y. X. Qi and L. W. Yin, *J. Mater. Chem.*, 2012, **22**, 16640.

9 J. Gao, M. A. Lowe and H. D. Abruña, *Chem. Mater.*, 2011, **23**, 3223.

10 Z. C. Bai, Z. C. Ju, C. L. Guo, Y. T. Qian, B. Tang and S. L. Xiong, *Nanoscale*, 2014, **5**, 3268.

11 F. Han, D. Li, W. C. Li, C. Lei, Q. Sun and A. H. Lu, *Adv. Funct. Mater.*, 2013, **23**, 1692.

12 J. Jiang, Y. Y. Li, J. P. Liu, X. T. Huang, C. Z. Yuan and X. W. Lou, *Adv. Mater.*, 2012, **24**, 5166.

13 Z. C. Bai, N. Fan, Z. C. Ju, C. L. Guo, Y. T. Qian, B. Tang and S. L. Xiong, *J. Mater. Chem. A*, 2013, **1**, 10985.

14 S. Z. Huang, J. Jin, Y. Cai, Y. Li, H. Y. Tan, H. E. Wang, G. V. Tendeloo and B. L. Su, *Nanoscale*, 2014, **6**, 6819.

15 Q. Hao, J. P. Wang and C. X. Xu, *J. Mater. Chem. A*, 2014, **2**, 87.

16 W. Xiao, J. S. Chen and X. W. Lou, *CrystEngComm*, 2011, **13**, 5685.

17 V. A. M. Brabers, S. F. M. Van and P. S. A. Knapen, *J. Solid State Chem.*, 1983, **49**, 93.

18 N. Tian, Z. Y. Zhou, S. G. Sun, Y. Ding and Z. L. Wang, *Science*, 2007, **316**, 732.

19 S. Devaraj, H. Y. Liu and P. Balaya, *J. Mater. Chem. A*, 2014, **2**, 4276.

20 C. C. Hu, Y. T. Wu and K. H. Chang, *Chem. Mater.*, 2008, **20**, 2890.

21 W. X. Zhang, Z. H. Yang, S. P. Tang, X. Z. Han and M. Chen, *J. Cryst. Growth*, 2004, **263**, 394.

22 R. Regmi, R. Tackett and G. Lawes, *J. Magn. Magn. Mater.*, 2009, **321**, 2296.

23 Y. Li, H. Y. Tan, X. Y. Yang, B. Goris, J. Verbeeck, S. Bals, P. Colson, R. Cloots, G. V. Tendeloo and B. L. Su, *Small*, 2011, **7**, 475.

24 H. Jahn and E. Teller, *Proc. R. Soc. London, Ser. A*, 1937, **161**, 220.

25 L. Wang, Y. G. Shi, Z. Chen, Y. B. Qin, H. F. Tian, C. Ma, H. X. Yang and A. A. Belik, *Solid State Commun.*, 2013, **153**, 71.

26 R. Tackett, G. Lawes, B. C. Melot, M. Grossman, E. S. Toberer and R. Sehadri, *Phys. Rev. B: Condens. Matter Mater. Phys.*, 2007, **76**, 024409.

27 M. A. Lowe, J. Gao and H. D. Abruña, *J. Mater. Chem. A*, 2013, **1**, 2094.

28 L. Li, Z. P. Guo, A. J. Du and H. K. Liu, *J. Mater. Chem.*, 2012, **22**, 3600.

29 K. F. Zhong, X. Xia, B. Zhang, H. Li, Z. X. Wang and L. Q. Chen, *J. Power Sources*, 2010, **195**, 3300.

30 D. Pasero, N. Reeves and A. R. West, *J. Power Sources*, 2005, **141**, 156.

31 J. F. M. Oudenhoven, L. Baggetto and P. H. L. Notten, *Adv. Energy Mater.*, 2011, **1**, 10.

32 H. L. Wang, Y. Yang, Y. Y. Liang, G. Y. Zheng, Y. G. Li, Y. Cui and H. J. Dai, *Energy Environ. Sci.*, 2012, **5**, 7931.

33 T. Li, Y. Y. Wang, R. Tang, Y. X. Qi, N. Lun, Y. J. Bai and R. H. Fan, *ACS Appl. Mater. Interfaces*, 2013, **5**, 9470.

34 D. P. Dubal and R. Holze, *RSC Adv.*, 2012, **2**, 12096.

35 L. Ji, H. Zheng, A. Ismach, Z. Tan, S. Xun, E. Lin, V. Battaglia, V. Srinivasan and Y. Zhang, *Nano Energy*, 2012, **1**, 164.

36 Z. C. Bai, Z. C. Ju, C. L. Guo, Y. T. Qian, B. Tang and S. L. Xiong, *Nanoscale*, 2014, **5**, 3268.

37 X. L. Wu, Q. Liu, Y. G. Guo and W. G. Song, *Electrochem. Commun.*, 2009, **11**, 1468.

7254 | *J. Mater. Chem. A*, 2015, **3**, 7248–7254

This journal is © The Royal Society of Chemistry 2015